ACS Sustainable Chemistry & Engineering

Research Article

Cite This: ACS Sustainable Chem. Eng. 2019, 7, 17055−17064

pubs.acs.org/journal/ascecg

Amino Acids for the Sustainable Production of Cu_2O Materials: Effects on Morphology and Photocatalytic Reactivity

Catherine J. Munro,[†] Elise C. Bell,[†] Mary O. Olagunju,[†] Joshua L. Cohn,[‡] Elsayed M. Zahran,[†,§] Leonidas G. Bachas,[†] and Marc R. Knecht*[,†,∥]

[†]Department of Chemistry, University of Miami, 1301 Memorial Drive, Coral Gables, Florida 33146, United States

[‡]Department of Physics, University of Miami, 1320 Campo Sano Drive, Coral Gables, Florida 33146, United States

[§]Department of Chemistry, Ball State University, Muncie, Indiana 47306, United States

[∥]Dr. J. T. Macdonald Foundation Biomedical Nanotechnology Institute, University of Miami, UM Life Science Technology Building, 1951 NW Seventh Ave, Suite 475, Miami, Florida 33136, United States

Supporting Information

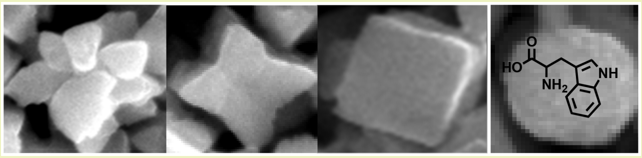

ABSTRACT: Photocatalytic technologies represent intriguing approaches for long-term environmental remediation strategies; however, approaches to sustainably generate the catalytic materials remain limited. Many methods require the use of toxic surfactants and potentially harsh conditions. As an alternative, bioinspired approaches present pathways toward the production of functional structures under ambient conditions. In this contribution, the effects of amino acids in the low-temperature production of Cu_2O-based materials is examined, providing first principle information for the eventual de novo design of peptides that can control the structure/function relationship of these inorganic materials. These studies demonstrate that only a fraction of the 20 canonical amino acids (Arg, Cys, Glu, His, Lys, and Trp) possess specific control over the morphology and size of Cu_2O materials during the synthetic process. This level of control is shown to directly affect the photocatalytic activity of the materials for the degradation of model organic pollutants. Taken together, these results provide intriguing new directions for the rational design of sustainable synthetic approaches for the production of catalytically important semiconductor metal oxide materials applied to long-term environmental remediation capabilities.

KEYWORDS: *Cu_2O, Amino acid, Photocatalytic degradation*

■ INTRODUCTION

Research into photocatalytic semiconductor materials is at the forefront today due to their relatively cheap syntheses and diverse applications in energy harvesting, photocatalysis, and environmental remediation, all of which are critically important for a sustainable future.[1−5] With a narrow band gap of ∼2.17 eV, Cu_2O is a p-type semiconductor that efficiently absorbs visible light making it advantageous for photocatalytic reactions compared to large band gap materials such as TiO_2, $SrTiO_3$, and ZnO, which are better suited for UV light absorption. Synthetic methods to generate Cu_2O vary widely allowing for the ability to fine-tune the final size and structure of the material.[6−9] Diverse architectures (spheres,[8] cubes,[5] octahedra,[6] wires,[10] 18-facet polyhedra,[11] etc.) have been produced using various surfactants[12] and ligands[13−15] through hydrothermal[8] and electrodeposition[16,17] methods. Further, recent work by Thoka et al. used sodium dodecyl sulfate with NaOH and sodium ascorbate to prepare Cu_2O nanocrystals at room temperature.[18] However, limited information exists concerning the effects of biologically relevant templates on the synthesis of Cu_2O. This is important because biological molecules allow for noncovalent interactions between the ligand and oxide materials that are known to alter oxide growth and final material structures and sizes under the ambient conditions exploited by nature.[19,20] In considering biological molecules as ligands for nanocrystal design, there is great potential to increase the relative green factor of material synthesis as well as alter the resulting photocatalytic properties.

While many studies have identified Cu^{2+} complexation with proteins and peptides,[21−24] few have looked at the peptide influence on Cu_2O synthesis.[25] Peptides have been previously isolated with affinity for Cu_2O.[26] Thai et al. used FliTrx cell-surface display methods to identify disulfide-constrained dodecapeptides with the ability to bind either ZnO or Cu_2O. For both peptides, Arg, Trp, and Gly were common residues in the metal oxide binding sequence, but Tyr, Pro, and Ser were generally underrepresented. Additionally, the peptides isolated for Cu_2O could be divided into two subclasses, where one class was hydrophilic with a high pI, and a second class that was hydrophobic with a low pI.[26] Integration of the CN225 peptide (RHTDGLRRIAAR), one of the identified Cu_2O binding sequences, into a larger protein structure was then exploited to generate Cu_2O-based nanorings, demonstrating the biomolecule's ability to direct material morpholgy.[27] Most recently,

Received: June 1, 2019
Revised: August 6, 2019
Published: October 10, 2019

DOI: 10.1021/acssuschemeng.9b03097
ACS Sustainable Chem. Eng. 2019, 7, 17055−17064

work by Wang et al. used these peptides, as well as others, to generate Cu_2O nanoparticles with octahedral, cubic, and spherical morphologies.[25] Here, His is the common residue in these peptides, where it is believed that His dictates Cu^{2+} complexation with the biomolecule.[28,29] These works together highlight that differences in peptide sequence may substantially alter the final material morphology and resultant properties. Unfortunately, minimal information is known about how the individual amino acids of the sequence affect the ability of the biomolecule to control the morphology and size of the final oxide material. By increasing the fundamental understanding of how each individual amino acid affects the Cu_2O synthetic process under green conditions, the design of new peptides with optimized sequences could occur to allow for fine-tuned selection of the oxide material size, structure, and optical properties. This could lead to rationally designed peptides for highly controlled production of Cu_2O structures with tailored properties.

Herein, we describe a sustainable synthesis approach to produce Cu_2O materials, where the influence of individual amino acids over the material morphology and photocatalytic properties is examined. Such information is critically important for the eventual de novo design of peptide sequences that could direct the fabrication of new Cu_2O structures with controlled morphologies and optical properties. The structures were prepared following a green hydrothermal method[8] at relatively low temperatures. Once prepared, the materials were characterized by scanning and transmission electron microscopies (SEM and TEM, respectively) to identify morphological differences due to the presence of each amino acid in the system. UV−vis diffuse reflectance spectroscopy (UV−vis DRS) and powder X-ray diffraction (XRD) were used to study the associated band gap and crystalline structure changes, respectively. From these analyses, most of the 20 canonical amino acids prepared a polydisperse set of Cu_2O morphologies; however, it is apparent that Arg, Cys, Glu, Lys, and Trp can exert significant control over the material morphology producing relatively uniform spherical structures of sizes between 350 and 900 nm. Interestingly, His, which has a well-known affinity for Cu^{2+}, results in the production of aggregated nanoclusters with features under 50 nm. To understand the photocatalytic properties of various structures, the spherical materials were tested for visible-light mediated degradation of organic dyes, which correlated to their available surface area in the reaction mixture. Interestingly, the catalytic capacities of the different materials varied widely, suggesting that the amino acid employed during material synthesis plays an important role in modulating the final properties of the materials. Taken together, these results demonstrate that, while specific amino acids may affect the final particle shape, different moieties may play a role in controlling the final optical and catalytic properties of the Cu_2O materials. By combining these characteristics, design principles could be developed to identify peptide sequences with the ability to control the morphology and properties of Cu_2O nanostructures.

■ EXPERIMENTAL SECTION

Materials. Anhydrous sodium carbonate and $CuSO_4{\cdot}5H_2O$ were purchased from BDH, while anhydrous D-(+)-glucose, methylene blue, and methyl orange were purchased from Alfa Aesar. Sodium citrate tribasic dihydrate along with L-valine, L-aspartic acid, L-phenylalanine, L-asparagine, L-alanine, L-glutamine, L-methionine, L-histidine, L-lysine, L-isoleucine, L-threonine, L-serine, L-tryptophan, L-arginine, L-tyrosine, and L-glutamic acid were obtained from Sigma-Aldrich. L-Proline, imidazole, and guanidine hydrochloride came from AMRESCO, while L-cysteine, glycine, and L-leucine were purchased from TCI. Absolute ethanol was acquired from Pharmco-AAPER. Aluminum and carbon specimen mounts for the SEM analysis and 400-mesh carbon-coated copper grids were purchased from EM Sciences. All reagents were used as received, and only ultrapure water (18.2 MΩ cm) was used in all experiments.

Particle Synthesis. Each amino acid−based particle synthesis was completed following a procedure adapted from previous protocols.[8] To a 25 mL capped glass vial with a magnetic stir bar, 6.59 mL of water, 6.00 mL of 1.0 mM aqueous amino acid solution, and 740.6 μL of 0.68 M aqueous $CuSO_4{\cdot}5H_2O$ were added. The resulting solution was a pale citrine blue and was stirred at 700 rpm for 10 min prior to the simultaneous and dropwise addition of 1.48 mL of 0.74 M sodium citrate and 1.48 mL of 1.22 M sodium carbonate resulting in a vibrant blue solution. Next, 3.70 mL of 1.4 M glucose was added and stirred for an additional 10 min prior to being placed in an oil bath for 2.0 h at 70 °C, where the reactions were constantly stirred. The solutions turned from the brilliant blue to an orange/red color within 25 min at the elevated temperature. After 2.0 h, the samples were filtered and washed using 1500 mL of water followed by 500 mL of absolute ethanol before being placed in a vacuum oven at 60 °C overnight.

SEM Analysis. SEM images of all materials were taken on an FEI XL-30 Field Emission ESEM/SEM operating at 20 kV. Each sample was prepared by suspending 1−5 mg of material in 200 μL of absolute ethanol. The suspension was sonicated for 5 min before 50 μL was extracted and drop-cast on the clean aluminum specimen mount. For His-derived materials, a carbon specimen mount was used to increase the resolution of the images of the material by eliminating aluminum charge effects. To identify the relative amount of each shape generated, a particle-shape analysis was performed by studying the morphologies of the first 100 particles over 10 images. After the shapes were identified, a size distribution for each shape was completed. Here, at least 100 particles of each shape were sized at their edge length for cubes and at their widest point for all other morphologies.

TEM Analysis. TEM analysis was performed for the His-directed Cu_2O material using a JEOL JEM-2010 microscope operating at 80 kV. The sample was prepared by drop-casting 5.0 μL of a diluted Cu_2O/ethanol suspension onto a carbon-coated 400 mesh Cu grid (EM Sciences) and allowed to dry overnight.

DRS Analysis. UV−vis DRS analysis was completed on a Shimadzu model UV-2600 system. The sample was prepared by filling a 2.0 mm quartz cuvette with ∼300 mg of the Cu_2O material so that when the sample was packed into the cuvette, it was at least 2/3 full. The spectrum of the sample was taken and converted into a Tauc plot before being analyzed using the Kubelka−Munk function, $F(R\infty)$, where the band gap values can be obtained from the tangent line of the Tauc plot. The quartz cuvette was cleaned with aqua regia to ensure residual material was eliminated before the analysis.

Powder XRD Analysis. Powder XRD analysis was completed on a Philips MRD X'Pert diffractometer using Cu Kα radiation. Samples were prepared on ozone cleaned glass slides, where at least 1 cm^2 was covered in a thin spread of vacuum grease before an even layer of the Cu_2O powdered material was added to the slide and analyzed.

BET Analysis. Characterization of the material surface area for select samples was performed by Brunauer−Emmett−Teller (BET) analysis. N_2 gas adsorption/desorption isotherms were obtained on an Autosorb iQ3 (Quantachrome) at 77 K. The samples were initially degassed at 50 °C under a vacuum system to remove any surface adsorbed species (e.g., water) for 24 h. The surface area for each sample was calculated using the desorption data in the BET classical range (0.05−0.3) with 11 points.

Dye Adsorption. The adsorption activity of the particles toward the model dyes methyl orange and methylene blue were studied to understand the rate of adsorption (absorbance of dye vs time) compared to its rate of degradation using previously established protocols.[30] In short, a stock suspension of 10.0 mg/mL of the Cu_2O materials was made in water and sonicated for 2 min. Next, 500.0 μL of the suspension (5.0 mg of particles) was added to 20.0 mL of dye with varying dye concentration from 20.0 to 1000.0 mg/L. A 150.0-μL aliquot was taken from each reaction at selected time points. The aliquot was centrifuged and the supernatant was analyzed on a Synergy|Mx Microplate reader, where a full spectrum was scanned in 1 nm increments, and the absorbance at 464 nm for methyl orange and 664 nm for methylene blue was tracked for each aliquot as a function of time. Each system was run in triplicate, and the values were then analyzed for their total percent adsorption. These data were also modeled using the Freundlich and Langmuir equations to understand if the mode of adsorption is influenced by the biomolecule template used in the synthesis.

Dye Degradation. The photocatalytic activity of the selected Cu_2O materials was examined using a previously established protocol.[6] In brief, a stock suspension of 10.0 mg/mL of the materials was made in water and sonicated for 2 min prior to use. When ready, 1.50 mL of the suspension (15.0 mg of the material) was put in a 100 mL glass crystallizing dish with 60.0 mL of 80.0 mg/L methyl orange or methylene blue. The system was covered with a quartz plate and immediately exposed to a 1000 W Xe arc lamp operating at ~100 mW/cm^2 in an Oriel Sol1A Class ABB solar simulator. The sample to light source distance was ~10 cm. Aliquots (150.0 μL) of the dye/particle mixture were taken at least every 15 min after the addition of particles for 4.0 h. Each 150.0-μL aliquot was placed in a microcentrifuge tube and spun at 14 000 rpm for 5 min before 100.0 μL of the supernatant was extracted and analyzed on a Synergy|Mx Microplate reader. For this, a full spectrum was scanned in 1 nm increments. The absorbances at 464 nm for methyl orange and 664 nm for methylene blue were tracked for each aliquot as a function of time to monitor the photodegradation process. The rate for each system was taken as an average of at least three trials with appropriate standard deviation.

RESULTS AND DISCUSSION

Understanding the interactions of amino acids in the synthesis of Cu_2O materials has the potential to identify how to manipulate both structural morphology and the resultant catalytic properties. This could lead to sustainable pathways toward design rules for biomediated production of these widely used photocatalytic materials. To analyze the effects of amino acids on the fabrication of Cu_2O materials, a standard synthetic approach was employed. In general, Cu^{2+} ions were slowly reduced to Cu^{+} using glucose in an aqueous solution containing the amino acid, sodium citrate, and sodium carbonate at 70 °C under constant stirring.[8] Using this protocol, the resulting materials displayed a wide range of colors spanning yellowish tones to deep brick reds based upon the amino acid employed during particle synthesis. These color disparities are potentially associated with varying metal oxidation states; however, crystal size and material shape may also alter sample colors.

To quantify the effects of the amino acid employed in the reaction on particle morphology, SEM and TEM imaging of the materials post purification were completed. An additional sample generated in the absence of any amino acid was also prepared and analyzed as a control system. In general, four different common morphologies were observed in the various samples that were prepared across the amino acids studied: spheres, cubes, stars, and bursts. Figure 1a−d present SEM images of examples of each shape to present the basis of the particle shape analysis. The sphere is shown in Figure 1a, where dimensions were measured based upon the diameter. The cube (Figure 1b) is identified as having rigid edges of generally equal length, width, and height, with its size measured by edge length. A star (Figure 1c) is similar to a cube but shows evidence of stretched corners and indentations along the particle edge with four defined extremities from a central core. A burst (Figure 1d) is similar to the star; however, it shows erratic extremities from all planes of the particle. For both the star and burst, dimensional analysis of the materials was completed based upon the longest tip-to-tip length of the structure.

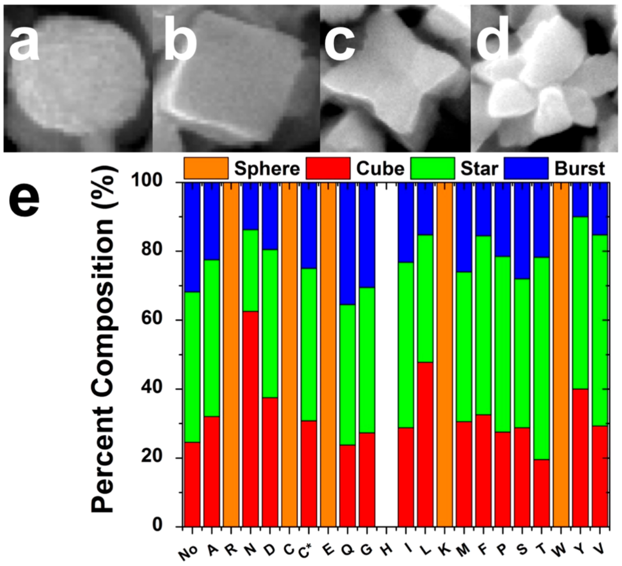

Figure 1. Particle shape analysis. Examples of the different shapes observed in the samples include (a) spheres, (b) cubes, (c) stars, and (d) bursts. Part (e) presents the shape distribution analysis for the Cu_2O materials prepared using the indicated amino acid. No refers to the ligand free control, while C* represents cystine.

From the analysis of the 22 samples studied, which include the amino acid free control and cystine as the oxidized form of cysteine, identification of the population of each shape (shown as a percentage of the whole) in the system was determined (Figure 1e). For the control sample prepared in the absence of any amino acid (SEM image shown in Figure 2a), three shapes were observed: cubes (25%), stars (44%), and bursts (31%). This control was selected to identify changes in shape distribution for the materials prepared using the amino acids. A difference between the control and any other material would suggest a shape-directing effect of the biomolecule over Cu_2O morphology (Figure 1e). For 14 of the amino acids (Ala, Asn, Asp, Gln, Gly, Iso, Leu, Met, Phe, Pro, Ser, Thr, Tyr, and Val), these species displayed particle shape distributions comparable to the amino acid free control. SEM analyses for these materials are shown in the Supporting Information, Figures S1−S21. Overall size distributions for the stars, bursts, and cubes for these samples are presented in Figure 2b−d. In general, these systems demonstrated no substantial control over material morphology or size, as compared to the amino acid free control, generating a mixture of cubes, stars, and bursts of similar population percentages and dimensions. While the percentages of the population of these different morphologies may vary to some degree from sample to sample, all three shapes were clearly observed in the system and generally reflect the control shape and size distributions.

When considering the measured sizes of the particles as a function of shape, it is interesting to note that the stars and bursts were similar in size and generally larger than the cubes. Overall, the cubes were on average <1.0 μm in edge length, while the stars and bursts were generally >1.0 μm in size. This

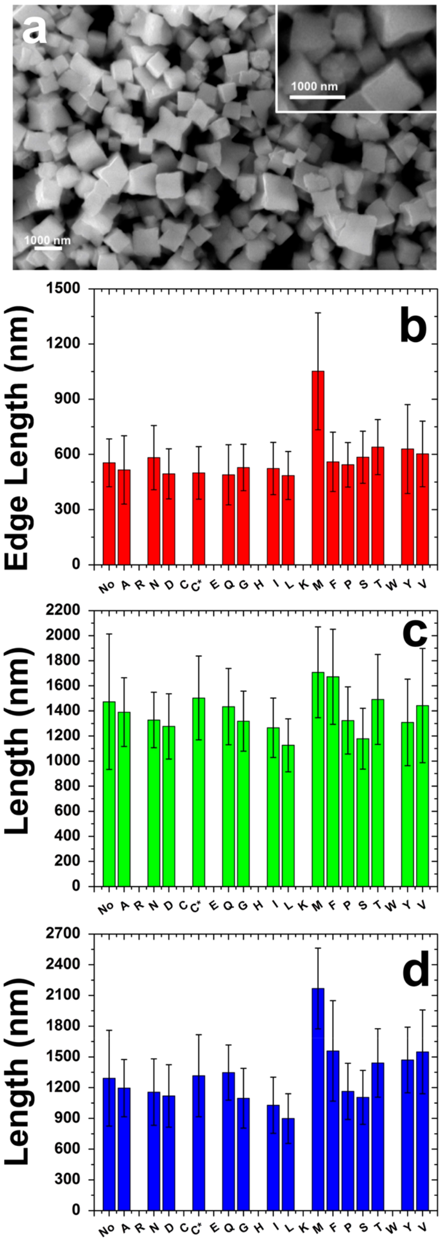

Figure 2. Particle shape and size analysis. Part a presents an SEM image of the control Cu_2O materials prepared in the absence of any amino acids. Parts b−d present the particle sizing analyses based upon the different shapes observed, including (b) cubes, (c) stars, and (d) bursts.

suggests that there may be an evolution of shape throughout the course of the reduction time. To better understand how these three shapes relate to each other, a time-based SEM analysis of the ligand-free synthesis was performed to understand the rate of growth for the cubes, stars, and bursts (Supporting Information, Figure S22). Here 45 batches of the no ligand material were prepared as described above and placed in an oil bath at room temperature while under constant stirring. Once the oil bath reached 70 °C, nine vials were pulled from the oil bath and filtered for SEM analysis. This was also done after 30, 60, 90, and 120 min of heating to identify material structural changes as a function of time. Over the course of the 2.0-h reduction process, the material population shifted from cubes (66%) and stars (34%) at the onset of the reaction, to cubes (33%), stars (56%), and bursts (11%) 60 min into the reduction process, and cubes (25%), stars (44%), and bursts (31%) at the end of the reaction. The progression of the material from cube to burst over the 2.0 h synthesis may be a result of Ostwald ripening on the initial cubes or star nanocrystals in the absence of a passivating agent or template.

While the clear majority of amino acids generated Cu_2O materials reminiscent of the control reaction performed without a biomolecule, noticeably different structures were generated when Arg, Cys, Glu, Lys, and Trp were present in the reaction system. These amino acids generated only spheres in the reaction mixture, which is highly distinct from the control system that did not generate any spherical structures. SEM images and particle sizing analyses of these materials can be seen in Figure 3. The smallest of the spherical structures is

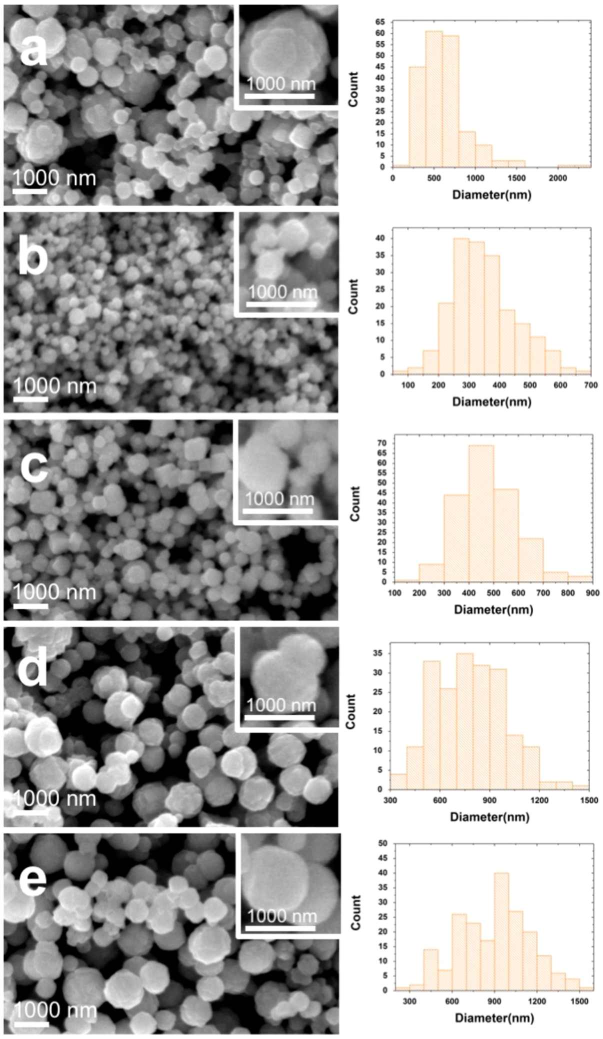

Figure 3. SEM analysis of the Cu_2O spheres generated in the presence of (a) Arg, (b) Cys, (c) Glu, (d) Lys, and (e) Trp. The SEM image of the material is presented on the left, while the particle size distribution histogram is shown on the right.

prepared using Cys with a diameter of 350 ± 106 nm. This small structure may be a result of the free thiol in Cys covalently binding with the Cu^{2+} in the synthetic process. Such a strong interaction could lead to smaller materials; however, additional analysis is required. As the amino acid employed in the reaction was altered across Glu, Arg, Lys, and Trp, the size of the Cu_2O spheres increased to 475 ± 122, 620 ± 298, 789 ± 211, and 898 ± 255 nm, respectively.

To monitor the growth of the spherical materials during the reaction, the Trp-based system was examined (Supporting Information, Figures S22 and S23). Using the same procedure described above, samples were examined at 0, 30, 60, 90, and 120 min into the heating/reaction time. Interestingly, compared to the no-ligand control, the only shape observed at all time points was spheres. The size of the spheres increased from 629 ± 197 nm at the onset of 70 °C to 898 ± 255 nm when the reaction was completed. No evidence of any nonspherical shape was noted, suggesting that the sphere-directing residues were able to directly manipulate and control the Cu_2O particle growth process throughout the reaction. This could be occurring at multiple steps in the process including modulation of the Cu^{2+} to Cu^+ reduction process, the rate of particle growth through surface adsorption, or some combination of these factors. Nevertheless, the spherical structures are a direct effect of the specific amino acid present in the reaction medium.

Because of the exposed free thiol, Cys has the potential to oxidize to the dimer cystine (labeled as C*). Such changes may directly manipulate the interaction of Cys with the growing metal oxide material in solution, providing important information on such effects. To probe this, the material synthesis process was repeated with cystine as the representative biomolecule. Remarkably, SEM analysis of the cystine-based materials demonstrated the production of stars (44%), cubes (31%), and bursts (25%). Such a shape distribution is reminiscent of the amino acid free control synthesis, strongly indicating that the free Cys structure is highly important in controlling the spherical Cu_2O morphology.

All of the Cu_2O structures discussed above are >100 nm, making their analysis accessible by SEM; however, the materials prepared in the presence of His were substantially smaller. Figure 4 presents an SEM and TEM image of the oxide materials generated using the imidazole-containing amino acid. For SEM analysis, a carbon mount was employed to eliminate aluminum charging effects and enhance the resolution of the His-based structures. Figure 4a presents the SEM image of the materials, where a clear mixture of larger structures dispersed with substantially smaller materials is evident. While the larger structures appear to be mixtures of different shapes, including cubes, bursts, and stars, the smaller materials seemed to be spherical in morphology. When these smaller Cu_2O particles were analyzed using TEM (Figure 4b), the analysis demonstrated that the oxide structure was generally spherical and partially aggregated with features on the order of ~50 nm in dimension. Unfortunately, due to the aggregated state of the materials, an accurate particle size and shape analysis for the His-prepared Cu_2O could not be completed using the TEM images.

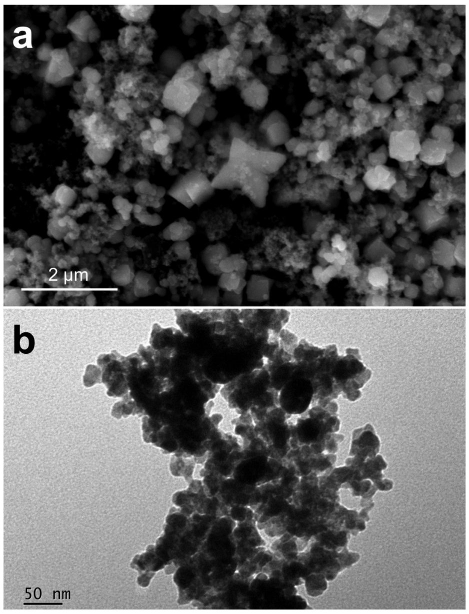

Figure 4. Particle analysis of the Cu_2O materials prepared using His by (a) SEM and (b) TEM.

While the His-prepared metal oxide materials were clearly aggregated, the small size of some of the structures indicates that the amino acid does influence the synthetic process, which is likely to be quite different from the other amino acids. Such effects are able to access Cu_2O morphologies of <100 nm, which could be translated into peptide sequence design. This size control may be due to the ability of His to act as a Lewis base and complex metal ions like Cu^{2+}, resulting in stronger interactions during the complexation step of the synthesis.[31] Such effects are likely to modulate Ostwald ripening throughout the fabrication process, thus altering the material size. In fact, Wang et al. previously reported similar coordination effects of His residues in peptide sequences for modulating the morphology of Cu_2O materials.[25]

As amino acids can change solution pH values, which could play a role in Cu_2O production, the pH of the reaction solution was determined after the addition of each reagent (Supporting Information, Figure S24). While differences in the pH were observed with the addition of the amino acid and copper sulfate, the pH of the final reaction mixture after the addition of sodium carbonate and sodium citrate stabilized to a pH range of 9.98 to 10.13. As such, during the glucose-based reduction process, the pH of the reaction was quite similar, regardless of the amino acid present in the synthesis. Therefore, it is unlikely that pH plays a significant role in Cu_2O structure determination.

SEM and TEM analysis of the amino acid-directed Cu_2O materials identified that different shapes and material sizes can be achieved based upon the biomolecule identity. To confirm that the final material composition was Cu_2O, as anticipated, powder XRD analysis of selected materials was completed. Due to the large number of samples (22 based upon the 20 amino acids, cystine, and amino acid free control), only five specific materials were characterized by this method. These include the samples made in the absence of any amino acid (i.e., the control), and those made in the presence of Arg, Cys, His, and Met (Figure 5a). These five samples were specifically selected to see if there is a difference in the crystallinity between sphere-directing amino acids (Arg and Cys), nonshape directing amino acids (Met), or His that shows size selectivity. Additionally, these samples probed all the different shapes (cubes, stars, bursts, and spheres) and sizes that were prepared, thus covering all the potential differences in the Cu_2O samples. When considering the materials prepared in the presence of Arg, only spherical Cu_2O particles were prepared. From the XRD analysis of this sample, diffraction peaks at 29.4, 36.3, 42.2, 61.4, 73.6, and 77.4°2θ were identified, which correspond to the (110), (111), (200), (220), (311), and (222) planes of

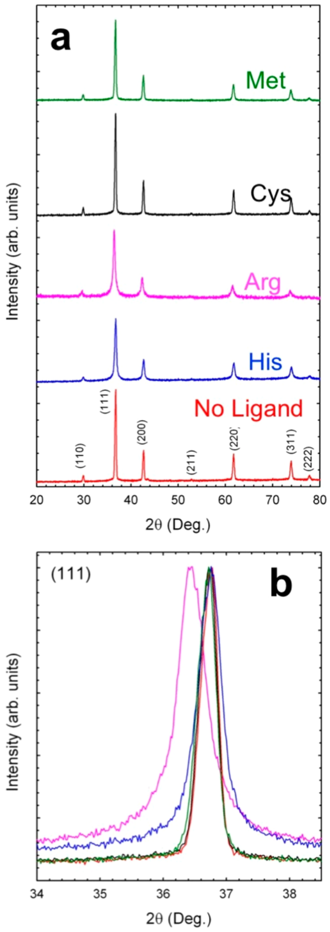

Figure 5. XRD analysis of the indicated materials. Part (a) presents the XRD patterns, while part (b) compares the normalized (111) reflections of the samples.

Cu_2O.[6] When the other materials were analyzed, an identical diffraction pattern was observed, including for the amino acid free control, confirming that the final materials were indeed composed of Cu_2O. Such a composition was expected based upon the synthetic approach, where the differences in particle shape and size were not affected by material composition, but were a result of the type of amino acid used in the reaction mixture.

While Figure 5a presents the diffraction patterns of the materials analyzed, Figure 5b compares the normalized (111) reflection of each material. From this analysis, it is evident that the samples prepared with Arg and His have notably broader reflections, indicating poorer crystallinity and/or smaller crystallite size as compared to the other samples. Use of the Scherrer equation implies a crystallite size for the Arg-based Cu_2O that is approximately a factor of 2 smaller than that of the amino acid free control specimen (17 nm vs 32 nm). Additionally, the reflection of the Arg sample is shifted to a lower angle by ∼0.3°. The 2θ values for the Arg sample best match literature values of bulk Cu_2O compared to the other samples tested. The reflections for all the other specimens imply a smaller lattice constant by ∼0.4% than the bulk value (0.427 nm).

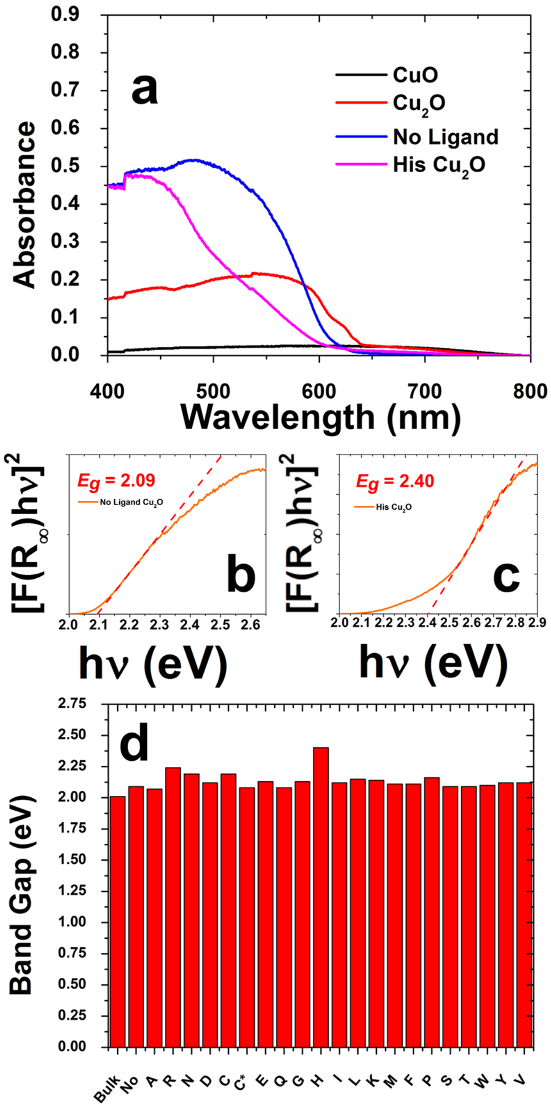

Figure 6. UV−vis DRS analysis of the Cu_2O materials. Part (a) presents the UV−vis spectra of the selected materials with Tauc plots for the amino acid free control and His-prepared samples shown in parts (b) and (c), respectively. Finally, part (d) compares the band gap energies for all samples.

With confirmation of the Cu_2O material composition from XRD, UV−vis DRS was performed to characterize the optical properties of the materials (Figure 6 and Supporting Information). Such a method can be used to quantify the band gap of the final structures, which is important to understand their photocatalytic properties. For this analysis, an additional control of commercially sourced bulk Cu_2O was studied. Using Tauc plots, a band gap of between 2.07 and 2.24 eV was noted for all of the materials prepared in the presence of the amino acids, except for the His-based Cu_2O materials that exhibited a band gap of 2.4 eV. These values are similar to the band gap for the bulk Cu_2O materials (2.01 eV) and for the control materials generated in the absence of the amino acid (2.09 eV). The changes for the materials prepared with the amino acids may arise from the minor contraction of the crystal structure, where the blue shift for the His-based materials is attributed to the quantum size effect arising from the substantially smaller particles that were prepared.[32]

Based upon the characterization analysis, it is likely that only specific amino acids can control the Cu_2O morphology, while most have negligible interactions with the growing oxide material. These amino acids are unlikely to have any noticeable effect on the particle growth process as they display materials of similar morphologies to the control sample prepared in the absence of amino acids. For those biomolecules that generated oxide structures with shape and size distributions that diverged from the amino acid free control, it is likely that they follow different paths for controlling the particle structure. To this end, only six amino acids could generate final materials of a single morphology or with specific size control: Arg, Cys, Glu, His, Lys, and Trp. As such, it is likely that these six residues have the strongest degree of interaction with the growing materials in the synthesis, potentially arresting growth in specific directions to prepare the specific size or spherical morphology. These biomolecules likely modulate the growth process of the Cu_2O in the reaction using various interactions including those with the Cu^{2+} and Cu^{+} ions throughout the reduction process.

The distinguishing factor between amino acids is their side chain, thus the differences in material morphology may arise from these functional groups. To probe these effects, Cu_2O synthesis was processed using guanidine and imidazole, which represent the side chains of Arg and His, respectively (Supporting Information, Figure S25). Interestingly, when using guanidine, spherical materials were generated with a size of 685 ± 164 nm, which is nearly identical to the size of the materials prepared using Arg. However, when examining the materials prepared using imidazole, large Cu_2O structures were prepared of varying morphologies. To this end, spheres, stars, and bursts were observed in this sample with dimensions ∼500 nm and larger on average. Such changes in morphology are vastly different than the exceedingly small sized materials prepared using His. Taken together, these controls demonstrate that the side chain functional group is highly important in controlling the material structure, but that the functional groups attached to the α carbon may also play an important role, depending upon how the side chain functions during material synthesis. While these results provide information over potential structural and size control, variations in their adsorption and photocatalytic capabilities could also be selected for based upon the amino acid used in the synthesis.

Cu_2O is a well-known visible light photocatalyst with the ability to degrade small molecules, including environmental pollutants and organic dye molecules.[33,34] This capability is inherently controlled by the particle size, shape, facet exposure, and affinity of the pollutant to the catalyst. Recent efforts have also looked to understand differences in Cu_2O materials as molecular sponges compared to their photocatalytic capacities to better predict final properties.[30] To better understand how the sphere directing materials interact with model organic pollutants, for both molecular adsorption in the dark and photocatalytic degradation in the light, the materials were exposed to both methyl orange, an anionic dye, and methylene blue, a cationic dye. For comparison, the control no ligand material was also tested to see how shape selectivity may enhance material adsorption and/or degradation.

Adsorption of a model organic pollutant to a catalyst surface is often dictated by electrostatic interactions between the substrate and the catalyst. To understand the effects of adsorption as opposed to photocatalytic degradation, reaction vials with 5.0 mg of each Cu_2O material was dispersed in 20.0 mL of 80.0 mg/L methyl orange or methylene blue. At selected time points, aliquots were extracted, and the amount of dye remaining in solution was quantified using UV−vis. Figure 7a compares the percent dye adsorption for methyl orange for the selected Cu_2O materials over 4.0 h in the dark. Fitting on the data can then be exploited to extract first order rate constants (k_{ad}) to compare the rates of adsorption among the materials as well as the rate of degradation (k_{deg}). From this analysis, it is evident that the Cu_2O materials prepared using Glu demonstrated the least amount of dye adsorption with a k_{ad} value of $(3.4 \pm 1.0) \times 10^{-9}$ min^{-1}. This suggests that negligible adsorption of the methyl orange dye to these materials was occurring. When the Cys-, Lys-, Trp-, and Arg-based materials were studied, k_{ad} values of $(114 \pm 0.5) \times 10^{-5}$, $(246 \pm 6.9) \times 10^{-5}$, $(108 \pm 0.6) \times 10^{-5}$, and $(300 \pm 0.1) \times 10^{-5}$ min^{-1} were determined, respectively. Such values are larger than the Cu_2O control structures prepared without a biomolecule in the

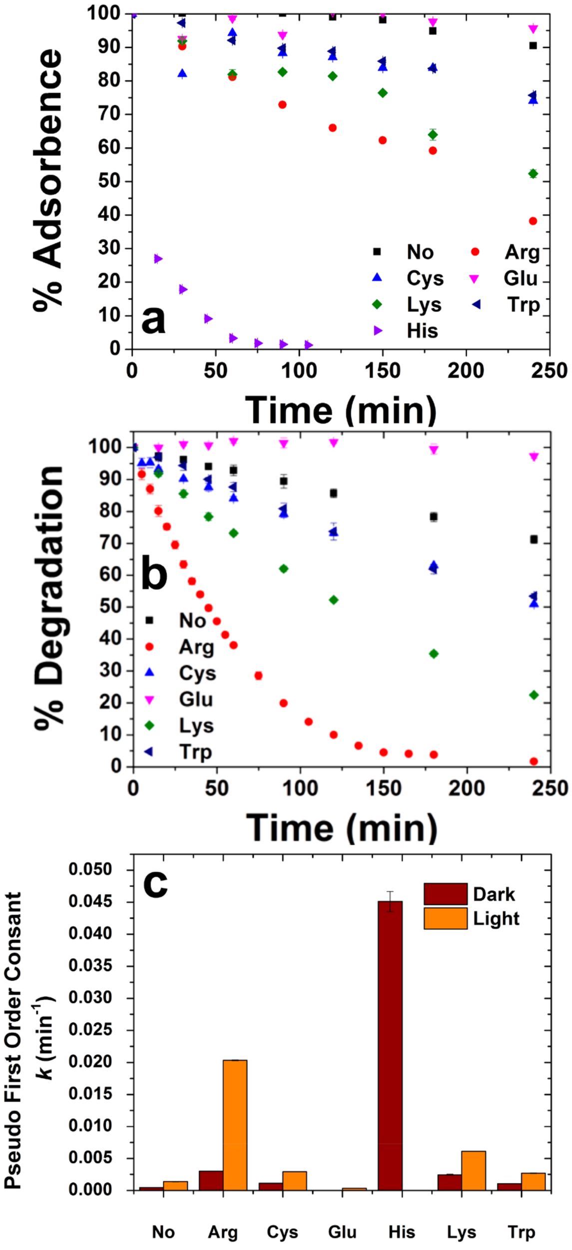

Figure 7. Photocatalytic analysis of the spherical Cu_2O materials for the degradation of methyl orange. Part (a) presents the dye adsorption study in the dark, while part (b) displays the percent dye degradation via photocatalysis. Part (c) compares the rate of dye adsorption (k_{ad}) to the rate of dye degradation (k_{deg}) where $k_{deg} > k_{ad}$ in all samples, demonstrating that the materials are photocatalytically degrading the model pollutant.

mixture, which gave rise to an adsorption rate constant of (42.9 ± 1.9) × 10^{-5} min^{-1}. Finally, maximum dye adsorption was observed for the Cu_2O particles prepared using His, which demonstrated a k_{ad} value of (4510 ± 158) × 10^{-5} min^{-1}. When the same experiment was completed in the presence of methylene blue, no adsorption was observed by UV−vis, consistent with previous work,[6] where no enhanced photocatalytic degradation of methylene blue was observed when exposed to pristine Cu_2O octahedra. In that study, Nguyen et al. reasoned that the exposed (111) facet of the octahedra presented a positively charged surface, resulting in electrostatic repulsion of the dye from the particles, limiting the photocatalytic effects.[6,34,35]

With a clear understanding of the rate of adsorption of methyl orange to the Cu_2O materials, the photodegradation capacity of the oxide structures was analyzed and compared (Figure 7b). Following a protocol similar to that of the adsorption studies, 15.0 mg of each Cu_2O material was dispersed in 60.0 mL of 80.0 mg/L methyl orange or methylene blue. Upon the addition of the dye to the Cu_2O, the suspension was immediately irradiated with a 1000 W Xe arc lamp operating at ∼100 mW/cm^2 in an Oriel Sol1A Class ABB solar simulator. At selected time points, aliquots were extracted and centrifuged. The supernatant was decanted, and the dye concentration was quantified using UV−vis. The materials were irradiated for 4 h to replicate the adsorption conditions, where the resulting data was fit using pseudo first order kinetic analysis. The results of the photodegradation study follow the same pattern as the adsorption study where the Glu-prepared oxide materials showed the least photodegradation with a k_{deg} value of (36.6 ± 0.2) × 10^{-5} min^{-1} and the Arg-based materials displayed the greatest reactivity with a k_{deg} value of (2030 ± 6.6) × 10^{-5} min^{-1}. The amino acid free control, Cys-, Lys-, and Trp-based Cu_2O materials displayed intermediate reactivity with rate constants of (139 ± 5.3) × 10^{-5}, (292 ± 3.2) × 10^{-5}, (611 ± 0.6) × 10^{-5}, and (268 ± 6.3) × 10^{-5} min^{-1}, respectively. Note that identification of the k_{deg} value for the His-based materials was not possible due to the rapid rate of dye adsorption. To this end, the dye was nearly completely adsorbed prior to light irradiation, preventing the catalytic analysis. In all cases, as shown in Figure 7c, the rate of dye degradation in the presence of light was substantially greater than the rate of dye adsorption to the Cu_2O surface (i.e., $k_{deg} > k_{ad}$), thus confirming that the materials are photocatalytically degrading the model organic pollutant.

From the results of Figure 7, notable differences in the adsorption and degradation capabilities are observed among the different Cu_2O materials, which does not directly correlate with particle shape or size. To better understand the adsorption properties of the selected metal oxide materials, two different analyses were conducted: BET analysis to quantify the reactive surface area and a saturation test[30] to determine if a monolayer or multilayer of dye was present on the oxide surface. Using standard BET analysis methods, the surface area of each material was quantified. These results indicated that the Cu_2O particles prepared in the presence of Arg have the highest reactive surface area (9.91 m^2/g). For all other amino acid-prepared structures, substantially smaller surface areas were quantified with values of 1.63, 2.16, 3.39, and 3.56 m^2/g for the Trp-, Glu-, Lys-, and Cys-based materials, respectively. Such values are comparable to the Cu_2O particles made in the absence of any amino acid (2.66 m^2/g). These results are consistent with the k values of adsorption and photocatalytic degradation, demonstrating the greatest reactivity for the Arg-based Cu_2O, which possessed a substantially greater surface area. For all other materials, the surface area is notably smaller than the Arg-based structures, resulting in greatly diminished reactivity. It is interesting to also note that those Cu_2O materials prepared with positively charged amino acids (Arg and Lys) tended to have the greatest adsorption and photocatalytic reaction rates with the negatively charged methyl orange dye. It is possible that residual positively charged species remain on the oxide surface, facilitating the adsorption process, leading to enhanced reactivity. This is further supported by the negatively charged amino acid (Glu) displaying the lowest degree of adsorption/reactivity. In this case, the negatively charged dye would be repulsed from the surface. Unfortunately, due to the size of the particles, zeta potential analysis of surface charge to explore further this hypothesis could not be conducted.

For the second adsorption study, a saturation test was conducted on all of the materials studied for photocatalytic reactivity. For this, 500.0 μL of a 10.0 mg/mL particle suspension was added to 20.0 mL of methyl orange dye with a concentration between 20.0 and 1000.0 mg/L, where multiple dye concentrations within this range were studied. After 48 h, a 150.0-μL aliquot was taken and centrifuged to remove the Cu_2O particles. The supernatant was then analyzed using UV−vis to quantify the amount of dye remaining in solution. The data was subsequently modeled using both the Freundlich and Langmuir isotherms separately to understand the adsorption mode of dye to the particle surface. In the fitting analysis, the no ligand control, as well as the Arg-, Cys-, Glu-, and Lys-prepared Cu_2O materials have better R^2 associations with the Langmuir model. This indicates that the dye more likely adsorbs as a monolayer to the solid surface for these structures. Interestingly, for the Trp-based materials, these structures were better fit with the Freundlich model (based upon R^2 values). These results suggest that the Trp-based structures have heterogeneous binding capabilities, which would likely lead to enhanced dye adsorption; however, based upon the BET analysis, they also show the smallest surface area, thus leading to diminished adsorption of dye molecules from solution.

When comparing the reactivity of the materials, it is important to take into account the sustainability of the material synthesis approach. Since photocatalytically reactive Cu_2O materials are prepared in the absence of any structure directing ligand, the reactivity of the materials must be substantially enhanced by a structure directing agent (e.g., the amino acids) to warrant inclusion in the synthesis. If the reactivity enhancement is negligible, then the addition of the amino acid would minimize its impact and increase the amount of waste from the system. In this specific case, the addition of Glu for Cu_2O preparation should be avoided as it leads to diminished k_{deg} values as compared to the materials prepared in the absence of amino acids; however, significantly enhanced reactivity is noted for the Arg-based Cu_2O structures. For these materials, their reactivity was >14-fold greater than the control structures. This level of enhancement is critically important to optimize the photocatalytic properties. Furthermore, the structure directing agent in this situation, Arg, is a nontoxic and naturally sourced ligand, thus enhancing its sustainable use in material synthesis.

Taken together, these results provide a fundamental level of understanding of the influence of amino acids on the synthesis and reactivity of Cu_2O materials. In this regard, six amino acids demonstrated a degree of morphology and size control over the growing Cu_2O materials: Arg, Cys, Glu, His, Lys, and Trp. From this, four key points can be extrapolated: specific amino acids can (1) influence the morphology and size of the oxide material during particle growth, (2) disrupt the crystallinity of Cu_2O material, potentially allowing for differences in the number of catalytic sites, (3) alter the catalytic properties of the final materials through variations in the reactive surface area, and (4) potentially vary the surface charge of the Cu_2O particles, altering the reactivity with charged reagents. Such capabilities were determined in comparison to amino acid-free control Cu_2O materials, confirming the effects of the individual biomolecules. Overall, Arg demonstrated the greatest effect over Cu_2O structure and properties providing spherical materials with the greatest level of reactivity.

It is interesting to note that the amino acids with some degree of control over Cu_2O particle morphology are similar to those residues well represented in peptide libraries identified with affinity for the oxide: Arg, Trp, His, and Gly.[26] While Gly was not demonstrated herein to alter particle morphology, both Arg and Trp were noted to prepare only spherical materials, while His was able to control the final material size. Furthermore, the residues that were generally underrepresented from the Cu_2O-binding peptides (Tyr, Pro, and Ser) expressed no observable ability to alter Cu_2O particle formation. These results may allow for eventual fine-tuning of peptide sequences to access enhanced control over the metal oxide structure/property relationship. Furthermore, these studies demonstrate that relatively facile analyses at the individual amino acid level can provide important information on the binding of peptides at material surfaces, especially for peptides identified with affinity for the target inorganic composition.

CONCLUSIONS

Herein, we have identified the effects of amino acids on both the sustainable production and reactivity of Cu_2O materials. In general, Arg, Cys, Glu, Lys, and Trp demonstrated shape selectivity over the final particle morphology, and His displayed a degree of control over particle size. These capabilities likely come from specific interactions between the growing oxide structure and the amino acid stabilizing Cu ions in solution and the final Cu_2O material surface. Beyond synthesis, the particles prepared using Arg displayed the greatest adsorption and photocatalytic reactivity for methyl orange degradation. Such capabilities are likely controlled by the interplay of the surface area and Cu_2O facets displayed to the dye solution. Taken together, these results provide a roadmap for the development of new peptides with the ability to sustainably produce Cu_2O with optimal photocatalytic reactivity for environmental remediation. While it is possible that differences in residue affinity are likely to occur when the amino acids are linked together in a peptide, these studies provide the first-principles for Cu_2O specific peptide design.

ASSOCIATED CONTENT

Supporting Information

The Supporting Information is available free of charge on the ACS Publications website at DOI: 10.1021/acssuschemeng.9b03097.

Additional SEM and TEM images of the Cu_2O materials, size distribution histograms of each material subdivided by shape, and Tauc plots of the materials prepared in the presence of different amino acids (PDF)

AUTHOR INFORMATION

Corresponding Author

*Phone: (305) 284-9351. E-mail: knecht@miami.edu.

ORCID

Joshua L. Cohn: 0000-0002-0702-9872
Leonidas G. Bachas: 0000-0002-3308-6264
Marc R. Knecht: 0000-0002-7614-7258

Notes

The authors declare no competing financial interest.

ACKNOWLEDGMENTS

We would like to thank the University of Miami for financial support of this research. C.J.M. acknowledges the University of Miami Dean's Summer Fellowship and the Dissertation Award for support in completing this work. J.L.C. acknowledges support by the U.S. Department of Energy, Office of Science, Office of Basic Energy Sciences, under Award No DE-SC0008607. Additionally, we would like to acknowledge the TEM Core at the University of Miami for microscopy analysis of our samples and the Herbert Wertheim College of Engineering Research Service Center at the University of Florida for BET analysis.

REFERENCES

(1) Liu, L.; Yang, W.; Li, Q.; Gao, S.; Shang, J. K. Synthesis of Cu_2O Nanospheres Decorated with TiO_2 Nanoislands, Their Enhanced Photoactivity and Stability under Visible Light Illumination, and Their Post-illumination Catalytic Memory. *ACS Appl. Mater. Interfaces* **2014**, *6*, 5629−5639.

(2) Wang, J.-C.; Zhang, L.; Fang, W.-X.; Ren, J.; Li, Y.-Y.; Yao, H.-C.; Wang, J.-S.; Li, Z.-J. Enhanced Photoreduction CO_2 Activity over Direct Z-Scheme α-Fe_2O_3/Cu_2O Heterostructures under Visible Light Irradiation. *ACS Appl. Mater. Interfaces* **2015**, *7*, 8631−8639.

(3) Li, J.; Cushing, S. K.; Bright, J.; Meng, F.; Senty, T. R.; Zheng, P.; Bristow, A. D.; Wu, N. Ag@Cu_2O Core-Shell Nanoparticles as Visible-Light Plasmonic Photocatalysts. *ACS Catal.* **2013**, *3*, 47−51.

(4) Haynes, K. M.; Perry, C. M.; Rivas, M.; Golden, T. D.; Bazan, A.; Quintana, M.; Nesterov, V. N.; Berhe, S. A.; Rodríguez, J.; Estrada, W.; Youngblood, W. J. Templated Electrodeposition and Photocatalytic Activity of Cuprous Oxide Nanorod Arrays. *ACS Appl. Mater. Interfaces* **2015**, *7*, 830−837.

(5) Zahran, E. M.; Bedford, N. M.; Nguyen, M. A.; Chang, Y.-J.; Guiton, B. S.; Naik, R. R.; Bachas, L. G.; Knecht, M. R. Light-Activated Tandem Catalysis Driven by Multicomponent Nanomaterials. *J. Am. Chem. Soc.* **2014**, *136*, 32−35.

(6) Nguyen, M. A.; Bedford, N. M.; Ren, Y.; Zahran, E. M.; Goodin, R. C.; Chagani, F. F.; Bachas, L. G.; Knecht, M. R. Direct Synthetic Control over the Size, Composition, and Photocatalytic Activity of Octahedral Copper Oxide Materials: Correlation Between Surface Structure and Catalytic Functionality. *ACS Appl. Mater. Interfaces* **2015**, *7*, 13238−13250.

(7) Yoon, S.; Kim, S.-D.; Choi, S.-Y.; Lim, J.-H.; Yoo, B. Hierarchical Shape Evolution of Cuprous Oxide Micro- and Nanocrystals by Surfactant-Assisted Electrochemical Deposition. *Cryst. Growth Des.* **2015**, *15*, 4969−4974.

(8) Sui, Y.; Fu, W.; Yang, H.; Zeng, Y.; Zhang, Y.; Zhao, Q.; Li, Y.; Zhou, X.; Leng, Y.; Li, M.; Zou, G. Low Temperature Synthesis of Cu_2O Crystals: Shape Evolution and Growth Mechanism. *Cryst. Growth Des.* **2010**, *10*, 99−108.

(9) Mishra, A. K.; Pradhan, D. Morphology Controlled Solution-Based Synthesis of Cu_2O Crystals for the Facets-Dependent Catalytic

Reduction of Highly Toxic Aqueous Cr(VI). *Cryst. Growth Des.* **2016**, *16*, 3688−3698.

(10) Chen, K.; Xue, D. Room-Temperature Chemical Transformation Route to CuO Nanowires toward High-Performance Electrode Materials. *J. Phys. Chem. C* **2013**, *117*, 22576−22583.

(11) Zhang, Y.; Deng, B.; Zhang, T.; Gao, D.; Xu, A.-W. Shape Effects of Cu_2O Polyhedral Microcrystals on Photocatalytic Activity. *J. Phys. Chem. C* **2010**, *114*, 5073−5079.

(12) Wang, W.; Tu, Y.; Zhang, P.; Zhang, G. Surfactant-Assisted Synthesis of Double-Wall Cu_2O Hollow Spheres. *Cryst. Eng. Comm.* **2011**, *13*, 1838−1842.

(13) Glaria, A.; Cure, J.; Piettre, K.; Coppel, Y.; Turrin, C.-O.; Chaudret, B.; Fau, P. Deciphering Ligands' Interaction with Cu and Cu_2O Nanocrystal Surfaces by NMR Solution Tools. *Chem. - Eur. J.* **2015**, *21*, 1169−1178.

(14) Azimi, H.; Kuhri, S.; Osvet, A.; Matt, G.; Khanzada, L. S.; Lemmer, M.; Luechinger, N. A.; Larsson, M. I.; Zeira, E.; Guldi, D. M.; Brabec, C. J. Effective Ligand Passivation of Cu_2O Nanoparticles through Solid-State Treatment with Mercaptopropionic Acid. *J. Am. Chem. Soc.* **2014**, *136*, 7233−7236.

(15) Theja, G. S.; Lowrence, R. C.; Ravi, V.; Nagarajan, S.; Anthony, S. P. Synthesis of Cu_2O Micro/Nanocrystals with Tunable Morphologies using Coordinating Ligands as Structure Controlling Agents and Antimicrobial Studies. *Cryst. Eng. Comm.* **2014**, *16*, 9866−9872.

(16) Yang, Y.; Han, J.; Ning, X.; Cao, W.; Xu, W.; Guo, L. Controllable Morphology and Conductivity of Electrodeposited Cu_2O Thin Film: Effect of Surfactants. *ACS Appl. Mater. Interfaces* **2014**, *6*, 22534−22543.

(17) Lee, S.; Liang, C.-W.; Martin, L. W. Synthesis, Control, and Characterization of Surface Properties of Cu_2O Nanostructures. *ACS Nano* **2011**, *5*, 3736−3743.

(18) Thoka, S.; Lee, A.-T.; Huang, M. H. Scalable Synthesis of Size-Tunable Small Cu_2O Nanocubes and Octahedra for Facet-Dependent Optical Characterization and Pseudomorphic Conversion to Cu Nanocrystals. *ACS Sustainable Chem. Eng.* **2019**, *7*, 10467−10476.

(19) Emami, F. S.; Puddu, V.; Berry, R. J.; Varshney, V.; Patwardhan, S. V.; Perry, C. C.; Heinz, H. Prediction of Specific Biomolecule Adsorption on Silica Surfaces as a Function of pH and Particle Size. *Chem. Mater.* **2014**, *26*, 5725−5734.

(20) Limo, M. J.; Ramasamy, R.; Perry, C. C. ZnO Binding Peptides: Smart Versatile Tools for Controlled Modification of ZnO Growth Mechanism and Morphology. *Chem. Mater.* **2015**, *27*, 1950−1960.

(21) Haas, K. L.; Putterman, A. B.; White, D. R.; Thiele, D. J.; Franz, K. J. Model Peptides Provide New Insights into the Role of Histidine Residues as Potential Ligands in Human Cellular Copper Acquisition via Ctr1. *J. Am. Chem. Soc.* **2011**, *133*, 4427−4437.

(22) Pires, M. M.; Przybyla, D. E.; Rubert Pérez, C. M.; Chmielewski, J. Metal-Mediated Tandem Coassembly of Collagen Peptides into Banded Microstructures. *J. Am. Chem. Soc.* **2011**, *133*, 14469−14471.

(23) Ginotra, Y. P.; Ramteke, S. N.; Srikanth, R.; Kulkarni, P. P. Mass Spectral Studies Reveal the Structure of $A\beta 1-16-Cu^{2+}$ Complex Resembling ATCUN Motif. *Inorg. Chem.* **2012**, *51*, 7960−7962.

(24) Gunderson, W. A.; Hernández-Guzmán, J.; Karr, J. W.; Sun, L.; Szalai, V. A.; Warncke, K. Local Structure and Global Patterning of Cu^{2+} Binding in Fibrillar Amyloid-β [$A\beta(1-40)$] Protein. *J. Am. Chem. Soc.* **2012**, *134*, 18330−18337.

(25) Wang, C.; Zhang, L.; Yang, J.; Wang, D.; Sun, Y.; Wang, J. Cuprous Oxide Nanostructures Tuned by Histidine-Containing Peptides and their Photocatalytic Activities. *Appl. Surf. Sci.* **2018**, *453*, 173−181.

(26) Thai, C. K.; Dai, H.; Sastry, M. S. R.; Sarikaya, M.; Schwartz, D. T.; Baneyx, F. Identification and Characterization of Cu_2O- and ZnO-Binding Polypeptides by *Escherichia coli* Cell Surface Display: Toward an Understanding of Metal Oxide Binding. *Biotechnol. Bioeng.* **2004**, *87*, 129−137.

(27) Dai, H.; Choe, W.-S.; Thai, C. K.; Sarikaya, M.; Traxler, B. A.; Baneyx, F.; Schwartz, D. T. Nonequilibrium Synthesis and Assembly of Hybrid Inorganic−Protein Nanostructures Using an Engineered DNA Binding Protein. *J. Am. Chem. Soc.* **2005**, *127*, 15637−15643.

(28) Slocik, J. M.; Wright, D. W. Biomimetic Mineralization of Noble Metal Nanoclusters. *Biomacromolecules* **2003**, *4*, 1135−1141.

(29) Kumara, M. T.; Tripp, B. C.; Muralidharan, S. Self-Assembly of Metal Nanoparticles and Nanotubes on Bioengineered Flagella Scaffolds. *Chem. Mater.* **2007**, *19*, 2056−2064.

(30) Ho, W.; Tay, Q.; Qi, H.; Huang, Z.; Li, J.; Chen, Z. Photocatalytic and Adsorption Performances of Faceted Cuprous Oxide (Cu_2O) Particles for the Removal of Methyl Orange (MO) from Aqueous Media. *Molecules* **2017**, *22*, 677.

(31) Barnard, E. A.; Stein, W. D. *The Roles of Imidazole in Biological Systems*; Interscience Publishers, INC.: Fordham University: New York, NY, 2009; Vol. *187*.

(32) Law, M.; Goldberger, J.; Yang, P. Semiconductor Nanowires and Nanotubes. *Annu. Rev. Mater. Res.* **2004**, *34*, 83−122.

(33) Huang, W.-C.; Lyu, L.-M.; Yang, Y.-C.; Huang, M. H. Synthesis of Cu_2O Nanocrystals from Cubic to Rhombic Dodecahedral Structures and Their Comparative Photocatalytic Activity. *J. Am. Chem. Soc.* **2012**, *134*, 1261−1267.

(34) Ho, J.-Y.; Huang, M. H. Synthesis of Submicrometer-Sized Cu_2O Crystals with Morphological Evolution from Cubic to Hexapod Structures and Their Comparative Photocatalytic Activity. *J. Phys. Chem. C* **2009**, *113*, 14159−14164.

(35) Yang, S.; Zhang, S.; Wang, H.; Yu, H.; Fang, Y.; Peng, F. Facile Synthesis of Self-Assembled Mesoporous CuO Nanospheres and Hollow Cu_2O Microspheres with Excellent Adsorption Performance. *RSC Adv.* **2014**, *4*, 43024−43028.

DOI: 10.1021/acssuschemeng.9b03097
ACS Sustainable Chem. Eng. 2019, 7, 17055−17064